scientific reports

OPEN

Protodioscin enhances Methotrexate-induced senescence and senolytic activity in HepG2 liver cancer spheroids by modulating cell cycle regulators and the TGF-β/p-Smad2-4 signaling pathway

Alborz Jafaei Souq[1], Ali Ghanbari[2], Mohammad Reza Tabandeh[3,4], Touraj Zamir Nasta[2], Azita Faramarzi[5], Fatemeh Makalani[1] & Cyrus Jalili[2]✉

Protodioscin (PD) is a natural saponin with anti-inflammatory, anticancer, and metabolic regulatory properties. Senolytic agents, which selectively eliminate senescent cells, are gaining attention for enhancing cancer therapy. This study evaluated the senolytic potential of PD in 3D HepG2 spheroids subjected to Methotrexate (MTX)-induced senescence. Spheroids were generated using the hanging drop method with a 1:1 mixture of HepG2 medium and HFF1-conditioned medium. Senescence was induced with 6 µM MTX, followed by 24-h PD treatment at 1.6, 4, and 8.14 µM (10%, 25%, and 50% of IC_{50}). Cell viability was assessed via MTT; ROS, NO, and TGF-β levels via ELISA; apoptosis via Annexin V/PI; and cell death via Calcein-AM. Expression of p16, p21, p27, p53, and p-Smad2/4 was measured by Western blot, and β-Galactosidase activity was used as a senescence marker. PD dose-dependently reduced spheroid viability and, combined with MTX, significantly enhanced apoptosis, cell death, ROS, NO, β-Gal activity, and expression of p16, p27, and p53, while downregulating p-Smad2/4 and TGF-β compared to MTX treatment alone. These findings suggest that PD potentiates MTX-induced senescence through modulation of cell cycle regulators and inhibition of the TGF-β/p-Smad2/4 pathway, highlighting its potential as a senolytic adjuvant in liver cancer therapy.

Keywords Protodioscin, Cellular senescence, Senolytic activity, Apoptosis, Spheroids, HepG2 cells

Abbreviations
PD	Protodioscin
HCC	Hepatocellular Carcinoma
HepG2	Human Liver Cancer Cell Line
MTX	Methotrexate
HFF1	Human Foreskin Fibroblasts (cell line 1)
PolyHEMA	Poly (2–hydroxyethyl methacrylate
ROS	Reactive Oxygen Species
NO	Nitric Oxide
TGF–β	Transforming Growth Factor–beta

[1]Student Research Committee, Kermanshah University of Medical Sciences, Kermanshah, Iran. [2]Medical Biology Research Center, Health Technology Institute, Kermanshah University of Medical Sciences, Kermanshah, Iran. [3]Department of Biochemistry and Molecular Biology, Faculty of Veterinary Medicine, Shahid Chamran University of Ahvaz, Ahvaz, Iran. [4]Stem Cells and Transgenic Technology Research Center, Shahid Chamran University of Ahvaz, Ahvaz, Iran. [5]Fertility and Infertility Research Center, Health Technology Institute, Kermanshah University of Medical Sciences, Kermanshah, Iran. ✉email: cjalili@yahoo.com

SASP	Senescence–Associated Secretory Phenotype
SA–β–Gal	Senescence–Associatedβ–Galactosidase
CDKI	Cyclin–Dependent Kinase Inhibitor
p16	Cyclin–Dependent Kinase Inhibitor 2 A (INK4a)
p21	Cyclin–Dependent Kinase Inhibitor 1 (Cip1/Waf1)
p27	Cyclin–Dependent Kinase Inhibitor 1B (Kip1)
p53	Tumor Protein p53
EMT	Epithelial–to–Mesenchymal Transition
R-Smads	Receptor–Regulated Smads
MTT	3–(4,5–Dimethylthiazol–2–yl)–2,5–diphenyltetrazolium bro

Hepatocellular carcinoma (HCC) is one of the most serious types of gastrointestinal cancer and a leading cause of death in many countries. The number of people diagnosed with liver cancer is expected to rise[1]. Due to the liver's vital role in detoxification, protein synthesis, and nutrients metabolism, cancer affecting this organ can have severe consequences for overall human health[2]. Methotrexate (MTX) has been used in the treatment of HCC, either alone or in combination with other agents, due to its anti-proliferative effects. One of the major anti-cancer and anti-inflammatory mechanisms of methotrexate is the induction of cellular senescence, in which damaged cells stop dividing[3,4]. However, several reports suggest that while MTX can suppress tumor growth by inducing cellular senescence, this same process may contribute to chemotherapy resistance. Cellular senescence is a state of stable cell cycle arrest that can be triggered by various stressors, including chemotherapy. Senescent tumour cells, though growth-arrested, remain metabolically active and can persist in the tumour microenvironment, promoting inflammation, tumour progression, and eventual relapse. This dual effect poses a significant challenge in liver cancer therapy, highlighting the need for combinatory approaches that can target senescent cells to improve treatment outcomes[5]. While senescence serves as a tumour-suppressive mechanism by halting the proliferation of damaged cells, it also has a paradoxical role in cancer progression. Senescent tumour cells can persist in the tumour microenvironment and secrete a variety of pro-inflammatory and pro-tumorigenic factors collectively known as the senescence-associated secretory phenotype (SASP). This secretory profile can promote tumour relapse, metastasis, and resistance to further therapy. As a result, the accumulation of senescent cells following chemotherapy contributes to therapeutic resistance and poor clinical outcomes[6]. Senescent cells can alter the tumour microenvironment and provide the conditions for the growth and spread of new tumours due to their properties such as the secretion of cytokines, chemokines, and growth factors[7]. Secretion of growth factors and inflammatory cytokines such as IL-6, IL-8 and TNF-α from senescent cells stimulates tumour growth and cause tumour recurrence and metastasis. Cell cycle regulators such as p21/Cip1, p16/INK4a, p27/Kip1, and p53 play central roles in the induction and maintenance of cellular senescence. Senescence is typically initiated in response to various stressors such as DNA damage, oxidative stress, or oncogene activation. p53, a key transcription factor activated by DNA damage, promotes the expression of p21, a cyclin-dependent kinase inhibitor (CDKI) that halts the cell cycle at the G1/S checkpoint by inhibiting CDK2. Similarly, p16 and p27 inhibit CDK4/6 and CDK2 activity, respectively, preventing phosphorylation of the retinoblastoma protein (Rb) and thereby enforcing cell cycle arrest. These coordinated actions lead to a stable growth arrest characteristic of senescent cells. Notably, the upregulation of these CDKIs not only prevents cell proliferation but also reinforces the senescent[8,9]. Senescence-associated β-galactosidase (SA-β-Gal) is a lysosomal enzyme whose increased activity is a hallmark of cellular senescence, widely used to detect and quantify senescent cells in vitro and in vivo[10]. Recent studies in several malignancies have demonstrated that chemotherapeutic treatments can activate the SASP pathway in human colon cancer C85 cells, MTX treatment resulted in G_1/S cell cycle arrest, SA-β-Gal positivity, and elevated p21 expression. The process is p53-dependent and associated with DNA damage and altered nitric oxide signalling. Similar senescence-related changes such as enlarged cell morphology, γH2AX foci, and increased p53/p21 expression are observed in MCF-7 breast cancer cells after MTX exposure[6]. It has been reported that Dox treatment induced senescence in both populations, accompanied by an increase in the expression of stemness and the multidrug resistance genes and an inhibition of Wnt/β-catenin signaling Additionally, conditioned media from DOX-treated cells induces senescence in human induced pluripotent stem cell (hiPSC)-derived hepatocytes[11]. Transforming growth factor-beta (TGF-β) plays a dual role in cancer, acting as a tumour suppressor in early stages by inducing cell cycle arrest, apoptosis, and senescence, but promoting tumour progression in later stages through epithelial-to-mesenchymal transition (EMT), immunosuppression, and metastasis. Smad proteins are key signaling molecules that function downstream of serine/threonine kinase receptors and serve as signal transducers of TGFß pathway[12]. Smad2 and Smad3 are receptor-regulated Smads (R-Smads) that are activated by TGF-β/activin signaling through type I receptors, including ALK4, ALK5, and ALK7[13]. The TGF-β signaling pathway phosphorylates and activates Smad2 and Smad3 and forms a complex with Smad4, which activates transcription factors such as Snail, Slug, and Twist, thereby repressing epithelial genes such as E-cadherin and increasing mesenchymal characteristics[14]. This process is the basis of EMT and plays an important role in the invasion and metastasis of cancer cells. In the context of senescence, TGF-β contributes to the induction and maintenance of the senescent phenotype by upregulating cyclin-dependent kinase inhibitors such as p15/INK4b and p21/Cip1 via SMAD2/3 signaling. It is also a component of the SASP, creating a feedback loop that reinforces senescence but may also support a pro-tumorigenic microenvironment if senescent cells persist[15,16]. Senescent cells typically exhibit elevated levels of ROS, contributing to oxidative stress that maintains the senescent phenotype. This persistent oxidative stress can promote DNA damage and pro-inflammatory SASP, which in turn supports tumour progression and therapy resistance in cancer[17]. Persistent senescent cancer cells balance high ROS levels by upregulating antioxidants like SOD, catalase, and glutathione, enabling their survival and continued SASP activity, which supports cancer progression. This balance allows senescent cells to persist and promote cancer progression[18,19]. These findings

highlight the potential implications of therapy-induced senescence in promoting stemness and tumorigenicity in HCC and show the importance of considering senolytic strategies to eliminate the adverse effects of senescent cells in cancer treatment. Senolytics are drugs that specifically target and destroy senescent cells by several molecular pathways, including the induction of apoptosis, disruption of survival signaling, and modulation of senescence-associated secretory factors. One of the primary effects of senolytics is the induction of apoptosis in senescent cells, which are typically resistant to cell death due to the upregulation of anti-apoptotic proteins such as BCL-2, BCL-xL, or PI3K/AKT/mTOR pathway components[20,21]. Additionally, senolytic treatment has been shown to modulate the expression of key cell cycle regulators. While senescence is maintained by elevated levels of p16/INK4a, p21/Cip1, and p53, senolytics may up-regulate these inhibitors in the surviving cell population or shift the balance toward apoptotic signaling rather than sustained arrest Furthermore, TGF-β expression, a prominent component of SASP, is often reduced following senolytic treatment. Since TGF-β can reinforce the senescent phenotype and promote a tumour-supportive microenvironment, its downregulation by senolytics contributes to diminishing chronic inflammation and halting tumor-promoting signaling cascades[22]. Senolytic treatment often reduces TGF-β expression, a key SASP factor that reinforces senescence and supports tumour growth, thereby helping to lower inflammation and suppress tumour-promoting signals. Cascades[23,24]. Recent studies have also demonstrated that senolytic treatment decreases markers of oxidative damage and inflammation, thereby restoring cellular homeostasis and reducing cancer-promoting signals[25,26]. Natural products have increasingly been explored in recent years as adjuvants in combination cancer therapy both to mitigate MTX-associated toxicities and to potentiate its anticancer efficacy[27,28]. Several senolytic compounds, such as dasatinib, quercetin, and navitoclax, have been reported to enhance chemotherapy efficacy by targeting senescent cells through mechanisms including inhibition of anti-apoptotic proteins, disruption of survival signaling pathways, and modulation of the SASP[26,29,30]. Despite progress in understanding senescence in liver tumours, effective senolytic strategies targeting resistant cells are still under investigation. Thus, combining novel senolytics with drugs like MTX is essential to enhance liver cancer treatment. Protodioscin (PD) is a steroidal saponin compound found in plants such as milk thistle, asparagus, and fenugreek[31]. PD has been reported to exhibit various biological activities, including the reduction of dyslipidaemia, protection against metabolic-related cardiovascular and renal diseases, as well as anti-inflammatory, anticancer, neuroprotective, and fertility-enhancing effects[32–34]. Recent research has shown that PD exhibits anticancer activity against several cancer cell lines, including bladder, prostate, colon, and breast cancers and liver[35–37]. Yu et al. (2022) demonstrated that PD reduced cell viability and induced apoptosis in Huh-7, HepG2, PLC/PRF/5, SK-Hep-1, and HA22T/VGH hepatocellular carcinoma cell lines in a dose-dependent manner at concentrations ≥ 6 μM. Moreover, oral administration of PD (25–50 mg/kg) significantly suppressed SK-Hep-1 xenograft tumor growth and decreased Ki-67 expression without observable toxicity[38]. In addition, PD has been reported to induce G2/M phase cell cycle arrest and apoptosis in HepG2 cells through downregulation of Cyclin B1 and BCL2, along with upregulation of Bax, further supporting its role as an anti-mitotic and pro-apoptotic compound[39].

Spheroid-based 3D cell cultures offer a more accurate representation of in vivo tissue compared to 2D models. Recently, 3D liver spheroids have become valuable tools for studying liver cancer and assessing therapeutic responses due to their tumour-like microenvironment. The persistence of senescent cells following chemotherapy can promote tumour progression, metastasis, and resistance through the SASP pathway. Therefore, eliminating these cells using senolytic agents has emerged as a promising strategy to enhance the effectiveness of conventional cancer treatments. PD has shown anticancer properties in various tumour types, but its potential senolytic activity, in particular, in 3D spheroid model remains underexplored. This study aimed to investigate the senolytic potential of PD in methotrexate (MTX)-treated HepG2 spheroids, generated using a modified hanging drop method and co-cultured with HFF fibroblast-conditioned medium.

Materails and method
Cell culture
For this study, Human foreskin fibroblast; HFF1 (ATCC-SCRC-1041) and HepG2 cell line (HB-8065) were obtained from the Pasteur Institute of Iran. They were cultured in DMEM-HG(Dulbecco's Modified Eagle Medium- High Glucose) medium (Bioidea, Iran) supplemented with 10% fetal bovine serum (Biosera, France) and 1% penicillin/streptomycin antibiotic solution (Bioidea, Iran). The cells were maintained in a CO2 incubator (PadidehNogene, Iran) at 37 °C, 90% humidity, and 5% CO2. When the cells reached approximately 80% confluency, they were washed twice with PBS to remove residual medium and non-adherent cells. The cells were then detached using 0.25% trypsin-EDTA (Bioidea, Iran) and incubated at 37 °C for 5 min until fully detached. The tryps was neutralized by adding complete growth medium, and the cell suspension was centrifuged at 300 × g for 10 min. After discarding the supernatant, the cell pellet was resuspended in fresh medium. Viable cells were counted using trypan blue exclusion staining, and appropriate numbers of cells were either sub-cultured or used for further experiments.

Preparation of HFF1 cells conditioned medium
After counting the fresh viable HFF1 cells, 0.5×10^6 cells were cultured in T25 flasks (Sanifico, Sout Korea) in DMEM-HG medium with 1% antibiotic and 10% FBS for 72 h. After 72 h incubation, the cell culture medium was collected and centrifuged at 3000 × RPM for 5 min to remove any detached cells or debris. The clarified supernatant was then filtered through a 0.22 μm pore size syringe filter (Biofil Co, India) to ensure sterility. The filtered HFF-1 conditioned medium was used immediately by mixing it at a 1:1 ratio with DMEM-HG culture medium for spheroid formation.

Preparation of polyhema coated plates

Three-dimensional spheroids of HepG2 cells were generated using the hanging drop method on Poly (2-hydroxyethyl methacrylate) (PolyHEMA)-coated plates as described previously[40,41]. A 120 mg/mL stock solution of poly (2-hydroxyethyl methacrylate) (Poly-HEMA; Sigma, USA) was prepared by dissolving the polymer in 95% ethanol. The solution was incubated overnight at room temperature (20 °C) under constant stirring using a sterile magnetic stir bar to ensure complete dissolution. To prepare the working solution (5 mg/mL), 250 μL of the Poly-HEMA stock was diluted in 4.25 mL of 95% ethanol. To prepare poly-HEMA-coated plates, 50 μL of poly-HEMA stock solution was added to each well of a 96-well U-bottom plate (Greiner BioOne, Austria). The plates were then left to evaporate with lids on at room temperature inside a sterile hood for 72 h. Once completely dried, the plates are sealed with parafilm and stored at 4 °C. The plates were sterilized with UV light before use for 30 min.

Spheroid formation and evaluation

For generation of HepG2 spheroids, cells were trypsinized and re-suspended as a single-cell suspension at a density of 1×10^6 cells/ml in a 1:1 ratio of DMEM-HG and fibroblast-derived medium. Next, 200 μL of this suspension is pipetted into each well of the poly-HEMA-coated plate, followed by centrifugation at $220 \times g$ for 10 min. Plates are then incubated at 37 °C with 5% CO_2 to allow spheroid formation. Spheroid formation was examined for one week using inverted microscopy (KoreaTech, Sout Korea). The morphology and diameter of the formed spheroids were examined by inverted light microscopy at days 0, 2, 5, and 7. Spheroid size was evaluated by measuring spheroid diameter using Image J software (NIH, Bethesda, Maryland, USA). Spheroids with a diameter of approximately 150–200 μm with relatively smooth edges and a concentrated cell mass in the inner part were used for further experiments.

MTT assay

To determine the IC50 of MTX and PD (Cat Number: G0299, Sigma-Aldrich) in HepG2 cells, 3- [4, 5-dimethylthiazol-2-yl]−2, 5-diphenyl tetrazolium bromide (MTT) assay was performed. Freshly produced spheroids in 96-well plate (5 spheroids/well) were treated with different concentrations of MTX and PD (1–100 μM) for 24 h in DMEM-HG medium containing 1% antibiotics and 2% FBS at 37 °C, 5% CO2, and 95% humidity. PD was dissolved in dimethyl sulfoxide (DMSO) (Merck, Germany) to prepare a 100 X stock solution for treatment, with the final DMSO concentration in culture medium kept below 0.1% to avoid solvent cytotoxicity. Control cells were treated with vehicle solution alone (DMSO). After 24 h incubation and removing the culture medium, 100 μl of 0.5 mg/ml solution of MTT solution (Sigma Aldrich, St. Louis, MO, USA, Cat. No. M5655) was added to each well and incubated in the dark for 3 h at 37 °C. After the formation of formazan crystals, 100 μl of DMSO was added to each well and then incubated in darkness for 30 min. The absorbance of the samples was measured using a microplate reader (BioTek, USA) at 570 nm. The analysis was conducted using three separate experiments, each consisting of three duplicate wells. The cell viability percentage was calculated by the following formula:

$$(\%)\text{cell viability} = \text{absorbance of test group/absorbance of control group} \times 100$$

The IC_{50} values were determined using non-linear regression analysis (log [inhibitor] vs. response – variable slope) in Graph Pad Prism software version 9 (Graph Pad Software, San Diego, CA, USA), based on dose–response curves generated from MTT assay data.

Experimental groups

Twenty freshly formed HepG2 spheroids were placed in 24-well plates containing DMEM-HG medium for each group and subsequently treated with MTX and PD. Spheroids were treated simultaneously for 24 h with MTX at 50% of its IC_{50} concentration (6 μM), primarily to induce cellular senescence, and with PD at 10% (1.6 μM), 25% (4 μM), and 50% (8.14 μM) of its IC_{50} value (~ 16 μM). Doses were selected from preliminary 24 h dose response curves: PD at 10%, 25%, and 50% of its IC_{50} to assess concentration dependent effects below overt cytotoxicity, and MTX at ~ 50% IC_{50} to establish senescence for evaluating PD's senolytic actions. Prior to treatment, the culture medium was replaced with low-serum DMEM-high glucose (DMEM-HG) medium containing 2% FBS to enhance drug responsiveness. PD was dissolved in DMSO, and the final DMSO concentration was maintained below 0.1% in all experimental groups. All treatments were conducted in triplicate. At the end of the experiment, the entire contents of each well, including the spheroids and culture medium, were collected and centrifuged together at $1500 \times g$ for 5 min. Following centrifugation, the spheroids were pelleted while the culture medium was carefully separated and stored at −80 °C for subsequent biochemical analyses. The spheroid pellets were gently washed with PBS and either processed immediately or stored at −80 °C for further molecular and cellular assays.

Nitric oxide assay

The nitric oxide concentrations following treatment with MTX and PD were assayed sing Nitric Oxide Assay kit (Kia Zist, Iran) based on the Griess method as recommended by the manufacturer. The media collected from the spheroids were transferred to a clean microplate and incubated with equal volume of Griess Reagent on shaker at room temperature for 10 min to allow the Griess reaction to occur. To determine the NO level, the absorbance at 540 nm was recorded. To interpolate concentrations of NO, serial dilution of nitrite was prepared in serum free media and processed along with the media samples. A standard curve was drawn using the absorbance values of the standard solutions and their respective concentrations in Graph Pad prism. Protein concentration was measured using Bradford assay. Results were expressed as nmol/mg protein.

Measurement of the intracellular ROS level

The intracellular levels of reactive oxygen species (ROS) were measured using ROS assay kit (Kiazist, IRAN, KROS96) by using 2', 7'-dichlorodihydrofluorescein diacetate (DCFDA), a non-fluorescent dye that interacts with ROS to create fluorescent 2, 7-dichlorofluorescein (DCF). To determine the ROS level in cells, the spheroids were dissociated and stained with 1 mM DCFDA solution in PBS and incubated in 37 °C incubator for 30 min. Following the incubation, the cells were washed twice with 1X PBS and DCFDA fluorescence intensity was determined at 491 nm excitation and 516 nm emission using fluorescence microplate reader. The mean florescence intensity normalised with blank media. Results were normalized by protein concentration which assayed by Bradford method and expressed in relative to control group.

Measurement of TGFβ concentration

The TGFβ levels in media of spheroids were measured using human ELISA kit (Sunlong Biotech, China, SL1736Hu), according to the manufacturer's instructions. The results were expressed as pg/mg protein. All samples were run in one assay to avoid inter-assay variation. All assays were performed using three technical replicates. The limit of detection of TGFβ was 0.8 pg/ml. The intra-assay coefficient of variation was less than 10%.

SA-β-GAL staining

To assess senescence associated β-galactosidase (SAβ-Gal) activity in spheroids, β-Gal Assay Kit (Cell Signaling Technology, USA, Catalog No. 9860) was used according to the manufacturer's instructions. At the end of the experiment, the growth media and spheroids were carefully aspirated from the wells and transferred to a micro centrifuge tube. The spheroids were then centrifuged at $300 \times g$ for 5 min to pellet the spheroids. After centrifugation, the supernatant was carefully removed, and the spheroid pellet was resuspended in 250 μL of 1X fixative solution. The spheroids were fixed for 15 min at room temperature. After fixation, the spheroids were centrifuged again at $300 \times g$ for 5 min, and the supernatant was discarded. The spheroid pellet was then resuspended in 250 μL of the β-Gal staining solution, ensuring complete coverage of the spheroids. The spheroids were incubated at 37 °C in a dry incubator overnight. Following the incubation, the spheroids were gently placed on slides for examination. Images of the stained spheroids were captured using a light microscope under the ×10 objective lens (Olympus BH-2, Japan) equipped with a Digital Dino-Eye camera (AM7023, Taiwan) and Capture 2.0 software. For quantitative analysis, the intensity of the blue dye was assessed using ImageJ software.

Apoptosis assay using annexin V/PI staining

To determine the apoptosis rate in treated spheroids, the FITC Annexin V-FITC/PI apoptosis detection kit (Padza, Iran) was used[42,43]. At the end of the experiment, single-cell suspensions of spheroids were prepared using trypsin digestion as described previously to prepare single-cell suspensions for the Annexin V/PI assay, spheroids were first removed from the culture medium and transferred to a sterile 1.5 mL tube. They were washed with PBS to remove any residual medium. Next, the spheroids were digested with 250 μL of 0.25% Trypsin-EDTA (Bioidea, IRAN) enzyme solution and incubated at 37 °C for 15 min, with gentle shaking occasionally. The digestion process was monitored under a microscope, and once the spheroids were fully dissociated into single cells, enzymatic activity was neutralized by adding 400 μL of FBS. The cell suspension was then centrifuged at 1500 rpm for 5 min to pellet the cells, which were subsequently used for the apoptosis assay. The cells were washed twice with cold PBS and then resuspended in 1× binding buffer. The cells were stained for 15 min with Annexin V-FITC at room temperature in the dark. Afterward, PI was added, and the samples were analysed by flow cytometry (BD Biosciences FACS Canto II, San Diego, CA) within 15 min. The percentage distribution of viable, early apoptotic, late apoptotic, and necrotic cells was calculated using FlowJo software version 10 (Tree Star, Inc., USA).

Live/Dead cell viability assay

At the end of the experiment, the growth media and spheroids were carefully aspirated from the wells and transferred to a 1.5 ml micro centrifuge tube. The spheroids were then centrifuged at $300 \times g$ for 5 min to pellet the spheroids. Following centrifugation, the spheroids were stained using a live/dead staining method as described previously[44]. For each sample 500 μL of the Calcein-AM working solution (2 μM in PBS) and 50 μL of the PI (1 μg/mL in PBS) working solution were added to each well. The spheroids were then incubated with the staining solution at 37 °C for 1 min. After incubation, the spheroids were gently washed 2–3 times with PBS to remove excess dye. For imaging, the stained spheroids were transferred to a microscope slide and covered with a coverslip. The spheroids were visualized under a fluorescence microscope using appropriate filters: Calcein-AM (live cells) was visualized with excitation at 495 nm and emission at 515 nm (green fluorescence), while PI (dead cells) was visualized with excitation at 535 nm and emission at 617 nm (red fluorescence). For data analysis, live cells fluoresced green due to Calcein-AM staining, and dead cells fluoresced red due to PI staining. The images were analyzed using ImageJ software to quantify the populations of live and dead cells. The viability percentage of the spheroids was then calculated using the following formula.

$$\text{Cell Viability}(\%) = \frac{\text{Number of Live Cells}}{\text{Total Number of Cells}} \times 100$$

Western blot analysis

The expression of P16, P21, P27, P53, p-Smad2 and p-Smad4 proteins in spheroids exposed to MTX and PD were measured by western blot method. Following 24 h exposure to MTX and PD, the growth media and spheroids were carefully aspirated from the wells and transferred to a 1.5 ml micro centrifuge tube. The spheroids were

then centrifuged at 300 × g for 5 min to pellet the spheroids. The spheroids were lysed in 200 μl of lysis buffer (Tris-HCl 50 mM, NaCl 150 mM, Triton X-100 0.1%, NaF 1 mM) supplied with protease inhibitor cocktails (Sigma-Aldrich, MO, USA) for 30 min on ice. The protein concentration of the cell lysate was quantified using the Bradford protein assay. Proteins were denatured, and a total of 10 μg of protein was loaded onto a 10% SDS-PAGE gel for electrophoresis. The proteins were then transferred onto polyvinylidene fluoride (PVDF) membranes (Amersham, USA) and blocked overnight at 4 °C with 5% BSA (Sigma, USA) in Tris-buffered saline (TBS, Sigma, USA) containing 0.05% Tween-20 (Sigma, USA)., the membrane incubated with primary antibodies diluted 1:500 in blocking solution;; anti-P16 (#80772; Cell Signaling Technology, USA), P21 antibody ((#2947; Cell Signaling Technology, USA), P27 antibody (#3686; Cell Signaling Technology, USA), P53 antibody (#2524; Cell Signaling Technology, USA), phispho-Smad 2 antibody (12570-1-AP Proteintech, USA USA), phospho-Smad 4 antibody (102–15354, Ray biotech, USA) and GAPDH antibody (5174, Cell Signaling Technology, USA) for 2 h at room temperature. After three 15-min washes in Tris-buffered saline with Tween 20, membranes were incubated with an appropriate secondary antibody (#96232, Cell Signaling Technology, USA) conjugated to horseradish peroxidase diluted 1:1000 in blocking solution for 2 following three additional washes, protein reactivity was visualized using an ECL detection kit (Parstous, Iran). Protein loading was normalized to GAPDH immunoreactivity (D16H11; Cell Signaling Technology, USA). The blots were detected using the Fusion X chemiluminescence imaging system (Vilber, USA). Optical density analysis was performed using the Fusion X software and expressed as fold change to the control group.

Statistical analysis

All data was analysed using the Graph Pad Prism version 9 (Graph Pad Software, San Diego, CA, USA). All data are reported as mean ± SEM. The Shapiro-Wilk test was used to evaluate data normality or error variance equivalence. The statistical differences were applied among all groups by one-way analysis of variance (ANOVA) and Tukey multiple-comparison post hoc test. A statistically significant difference between different experimental groups was indicated as follows: *$p < 0.05$, **$p < 0.01$, *** $p < 0.001$, **** $p < 0.0001$.

Results

### Characteristics of HepG2 derived spheroids

The HepG2 spheroids were successfully formed on PolyHEMA-coated plates, with spheroid morphology and size monitored over a 7-day period. At day 2, spheroids began to form distinct structures with visible aggregation of cells, while by day 5, spheroids exhibited a more compact and well-formed structure with a smooth edge. By day 7, spheroids reached a diameter of approximately 150–200 μm, which was ideal for further experimental use (Fig. 1). The spheroids demonstrated consistent size and uniformity, indicating successful formation under the described conditions. These results highlight the effectiveness of the PolyHEMA-coated plates and the fibroblast-conditioned medium in promoting the uniform formation of HepG2 spheroids suitable for further analysis.

### Effect of PD and MTX on the cell viability of HepG2 derived spheroids

The effect of PD and MTX on the viability of HepG2 derived spheroids was examined using MTT assay. The results showed that PD and MTX dose-dependently suppressed cell viability in HepG2 derived spheroids. The IC50 values at 24 h were 12.25 μM and 16.28 μM for MTX and PD, respectively (Fig. 2A, B).
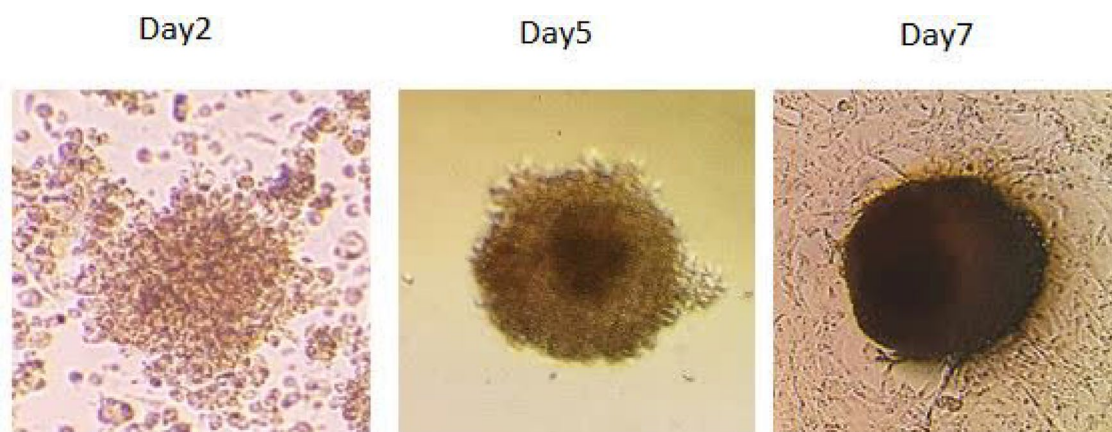
Fig. 1. Morphology of HepG2-derived spheroids on days 2, 5, and 7 after culture. On Day 2, cells begin to aggregate with loose and irregular boundaries. By Day 5, the spheroid becomes more compact, with partial boundary smoothing and increased cell-cell cohesion. By Day 7, a well-defined, dense, and nearly spherical structure with a smoother surface is observed, indicating maturation and stabilization of the spheroid architecture.
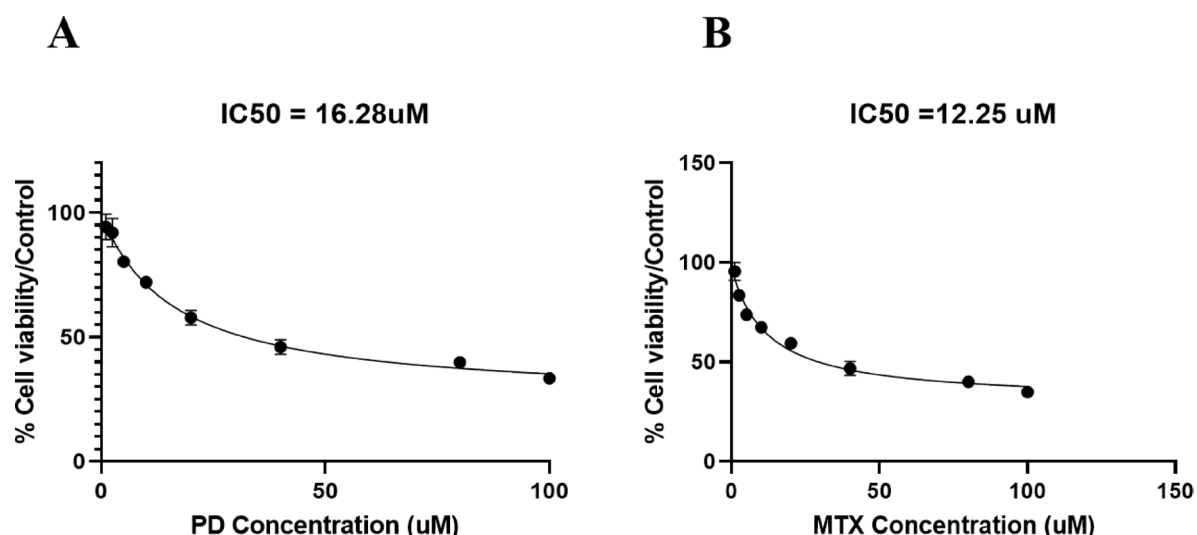
Fig. 2. Cytotoxic effects of Protodioscin (PD) and Methotrexate (MTX) on HepG2 derived spheroids. The spheroids were treated with different concentrations of PD and MTX (1–100 μM) for 12 h and the viability of spheroids was measured by MTT assay to determine the IC50 values. For control, the cells were treated with 0.2% DMSO (vol/vol) in the cell culture media, and the results from the control were used to normalize the data. Data represent the mean ± SD of three independent experiments.
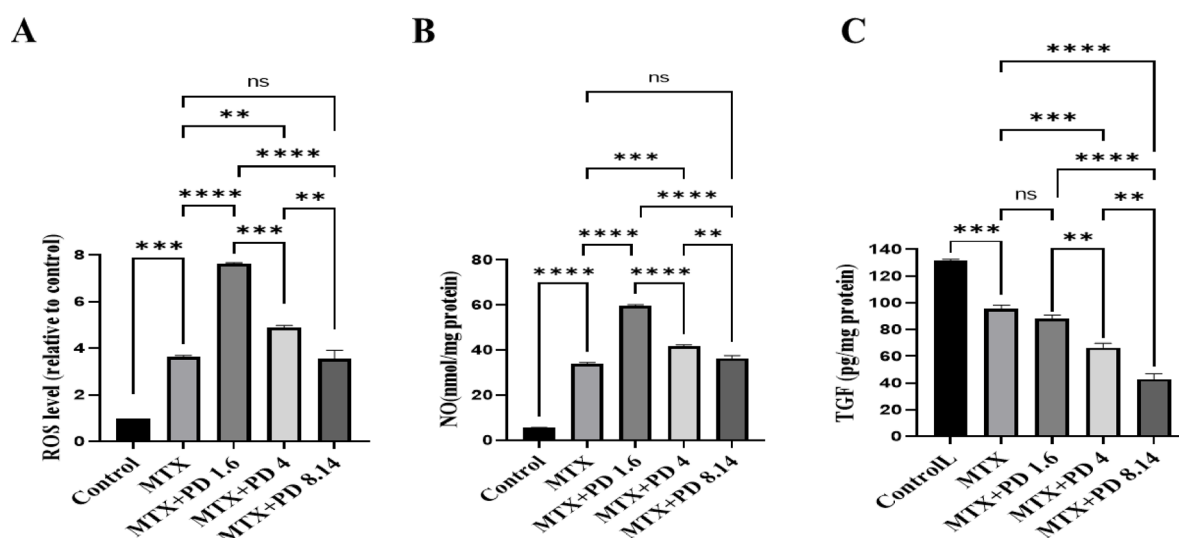
Fig. 3. The Levels of ROS (**A**), NO (**B**) and TGFß (**C**) in HepG2derived spheroids following Protodioscin (PD) and Methotrexate (MTX) treatment for 24 h. The results are reported as mean ± standard deviation. Control (control group), MTX (6 μm), MTX + PD 1.6 (6 μm MTX + 1.6μM PD), MTX + PD 4 (6 μm MTX + 4μM PD) and MTX + PD 8.4 (6 μm MTX + 8.14μM PD). **, *** and **** demonstrate significant difference between groups at $P < 0.01$, $p < 0.001$ and $p < 0.0001$.

Effect of PD and MTX on oxidative stress markers in HepG2 derived spheroids

The results showed that the levels of ROS were significantly increased in the MTX group compared to the control group ($p < 0.001$). Furthermore, ROS levels were significantly elevated in the 1.6 μM and 4 μM PD + MTX group compared to the MTX group ($p < 0.0001$ and $p < 0.01$, respectively) (Fig. 3A). There was no significant difference in ROS levels between the 8.14 μM PD + MTX group and the MTX group. The ROS levels was increased significantly in 1.6 μM PD + MTX group compared to the 4 and 8.14 μM PD + MTX groups ($p < 0.001$, $p < 0.0001$). (Fig. 3A).

The results showed that the levels of NO were significantly increased in the MTX group compared to the control group ($p < 0.0001$).Spheroids that treated with MTX in combination with 1.6, 4, and 8.14 μM PD showed significant elevation of NO release compared to the MTX group ($p < 0.0001$, $p < 0.01$). The NO level was

increased significantly in the 1.6 μM PD + MTX group compared to the 4 and 8.14 μM PD + MTX groups ($p < 0.01$, $p < 0.0001$((Fig. 3B).

Effect of PD and MTX on TGFß levels in HepG2derived spheroids

The results showed that TGFß levels were significantly decreased in the MTX group compared to the control group ($p < 0.001$).TGFß levels were reduced significantly in the 8.14 and 4 μM PD + MTX groups compared to the MTX group ($p < 0.0001$, $p < 0.01$). TGFß levels in the 1.6 μM PD + MTX group did not show any significant difference with the MTX group. The TGFß level was reduced significantly in the 8.14 μM PD + MTX group compared to the 1.6 and 4 μM PD + MTX groups ($p < 0.01$, $p < 0.0001$). (Fig. 3C).

Effect of PD and MTX on the Saβ-Gal activity in HepG2 derived spheroids

Senescence induction in HepG2 spheroids treated with PD and MTX was assessed by measuring SAβ-Gal activity The result showed that SAβ-Gal activity was significantly increased in HepG2-derived spheroids following MTX treatment compared with the control group ($p < 0.05$).The combination of MTX with PD at doses of 4 and 8.14 μM significantly increased the Saβ-Gal activity compared to the MTX alone group ($p < 0.00001$, (Fig. 4). PD at a dose of 1.6 μM had no significant effect on Saβ-Gal activity when combined with MTX, compared to the MTX-only treated group.

Effect of PD and MTX apoptosis of HepG2derived spheroids

The rate of apoptosis of HepG2-derived spheroids in different experimental groups is shown in Fig. 5A-B. The apoptosis rate of HepG2 derived spheroids was increased significantly in the MTX group compared with the control group ($p < 0.0001$). The combination of MTX with PD at doses of 4 and 8.14 μM significantly increased the apoptosis rate compared to the MTX alone group ($p < 0.0001$, $p < 0.01$). The rate of apoptosis was significantly higher in the 8.14 μM PD + MTX group compared to the 1.6 and 4 μM PD + MTX groups ($p < 0.05$, $p < 0.001$) (Fig. 5B).

Effect of PD and MTX on viability of HepG2derived spheroids

Live/dead cell imaging of spheroids treated with PD and MTX was performed using Calcein-AM/PI staining to determine cell viability (Fig. 6A). The results showed that the mean relative fluorescence intensity of PI—a marker of dead cells—in HepG2-derived spheroids was significantly increased in the MTX group compared to the control group ($p < 0.0001$). Furthermore, the combination of MTX with PD at doses of 1.6, 4 and 8.14 μM resulted in a significantly higher PI fluorescence intensity compared to the MTX group alone ($p < 0.0001$ and $p < 0.01$, respectively). The 8.14 μM PD + MTX group showed a significantly higher PI fluorescence intensity compared to the 1.6,and 4 μm PD + MTX group ($p < 0.0001$) (Fig. 6B).
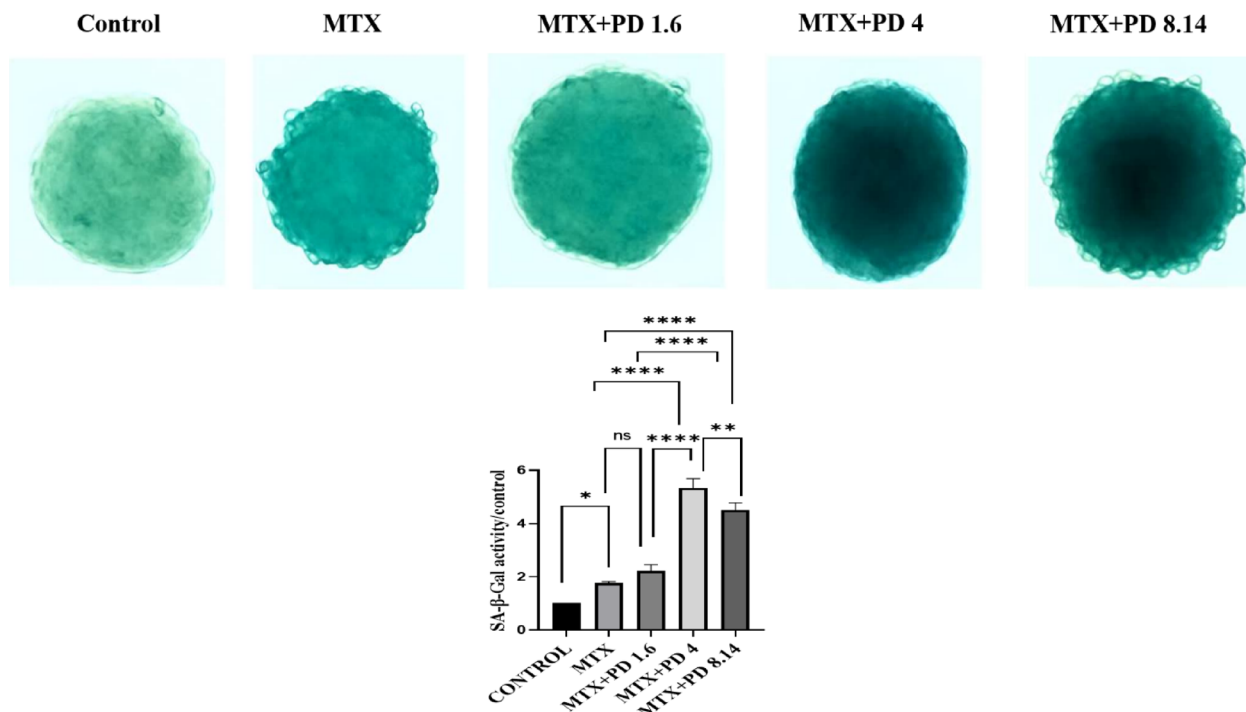
Fig. 4. The activity of senescence associated β-galactosidase activity in HepG2-derived spheroids following treatment with Protodioscin (PD) and Methotrexate (MTX) for 24 h. Control (control group), MTX (6 μm), MTX + PD 1.6 (6 μm MTX + 1.6μM PD), MTX + PD 4 (6 μm MTX + 4μM PD) and MTX + PD 8.4 (6 μm MTX + 8.14μM PD). The results are reported as mean ± standard deviation. *, ** and **** demonstrate significant difference between groups at $P < 0.05$, $p < 0.01$ and $p < 0.0001$.
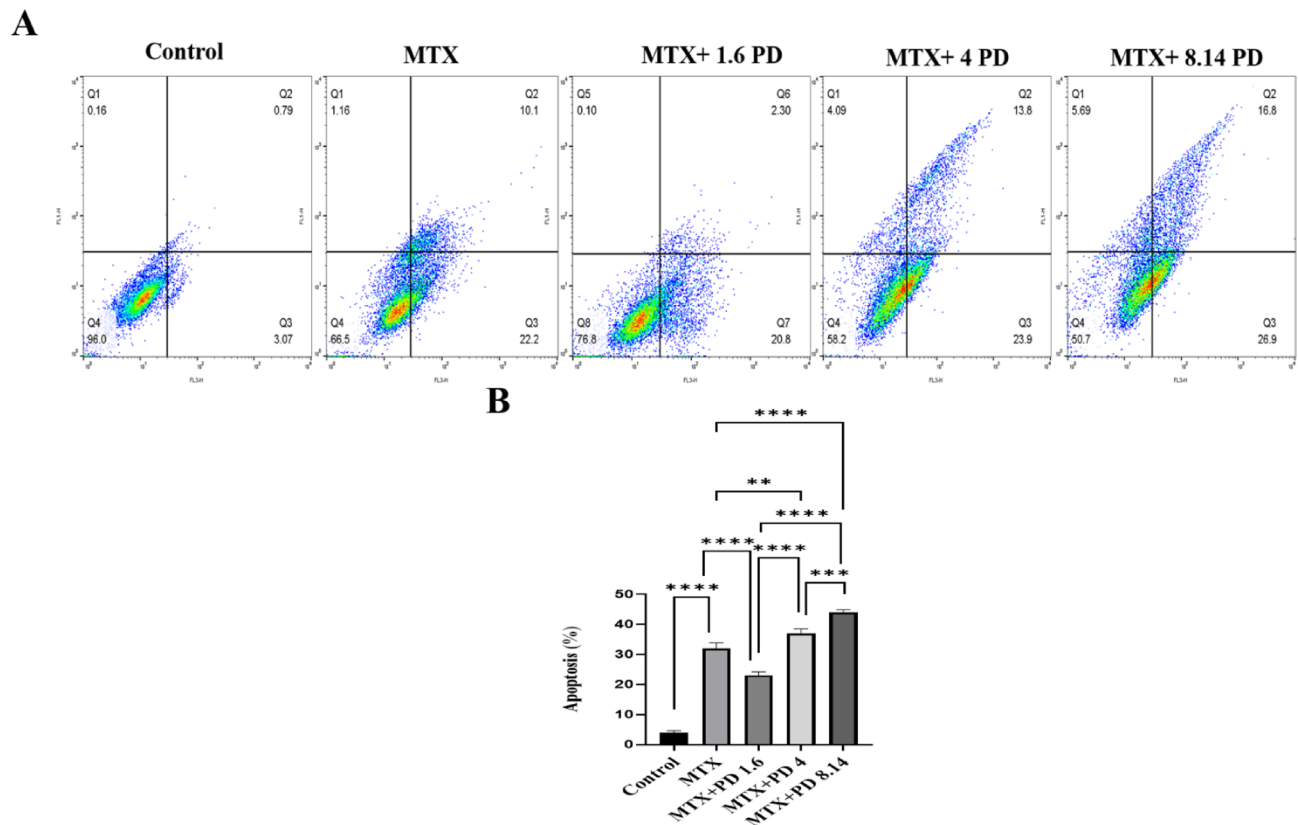
Fig. 5. Annexin V-FITC/PI staining of HepG2-derived spheroids following treatment with Protodioscin (PD) and Methotrexate (MTX). A Control (control group), MTX (6 μm), MTX + PD 1.6 (6 μm MTX + 1.6 μM PD), MTX + PD 4 (6 μm MTX + 4 μM PD) and MTX + PD 8.4 (6 μm MTX + 8.14μM PD). At least 10,000 cells were analysed per sample, and quadrant analysis was performed. A: Q1 necrosis, Q2 late apoptosis, Q3 early apoptosis, Q4 viable, B: All data are expressed as mean ± SEM. **, *** and **** demonstrate significant difference between groups at $P < 0.01$, $p < 0.001$ and $p < 0.0001$.

Effect of PD and MTX on the expression of cell cycle and senescence associated proteins in HepG2 derived spheroids

The Western blot analysis indicated that the expression of p16 protein was increased significantly in the MTX group compared to the control group ($p < 0.05$). Moreover, in the 1.6, 4, and 8.14 μM PD + MTX groups, p16 expression was further increased compared to the MTX group ($p < 0.0001$ and $p < 0.05$, respectively). The expression of p16 protein was significantly higher in the 8.14 μM PD + MTX group compared to 1.6 and, 4 μM PD + MTX groups ($p < 0.05$) (Fig. 7A).

The expression of p21 protein was increased significantly in the MTX group compared to the control group. ($P < 0.05$). Moreover, in the 4 and 8.14 μM PD + MTX groups, p21 expression was significantly higher than in the MTX group ($p < 0.0001$ and $p < 0.01$, respectively). The expression of p21 protein was increased significantly in the 8.14 μM PD + MTX group compared to 1.6 and 4 μM PD + MTX groups ($p < 0.0001$, $p < 0.001$) (Fig. 7B).

The expression of p53 protein in the MTX group did not significantly change compared to the control group. In the 1.6, 4, and 8.14 μM PD + MTX groups, the expression of p53 proteins were significantly increased compared to the MTX group ($p < 0.0001$, $p < 0.01$, $p < 0.05$, respectively). The expression of p53 protein was increased significantly in the 8.14 μM PD + MTX group compared to 1.6, and 4, μM PD + MTX groups ($p < 0.05$, $p < 0.01$) (Fig. 7C).

The expression of p27 protein in the MTX group did not significantly change compared to the control group. In the 1.6, 4, and 8.14 μM PD + MTX groups, the expression of p27 protein were significantly increased compared to the MTX group ($p < 0.0001$, $p < 0.05$). The expression of p27 protein was significantly higher in the 8.14 μM PD + MTX group compared to the 1.6 μM PD + MTX group ($p < 0.01$) and had no significant difference with 4 μM PD + MTX group ($p < 0.05$, $p < 0.01$) (Fig. 7D).

Effect of PD and MTX on the expression of TGFβ pathway-related proteins in HepG2-derived spheroids

The expression level of p-Smad2 protein in the MTX group was significantly decreased compared to the control group ($p < 0.01$). In the 4 and 8.14 μM PD + MTX groups, the expression of p-Smad2 was reduced significantly compared to the MTX group ($p < 0.05$). The expression of p-Smad2 protein in the 1.6 μM PD + MTX group did not show any significant difference with MTX group. The expression of p-Smad2 protein in the 1.6 μM PD + MTX
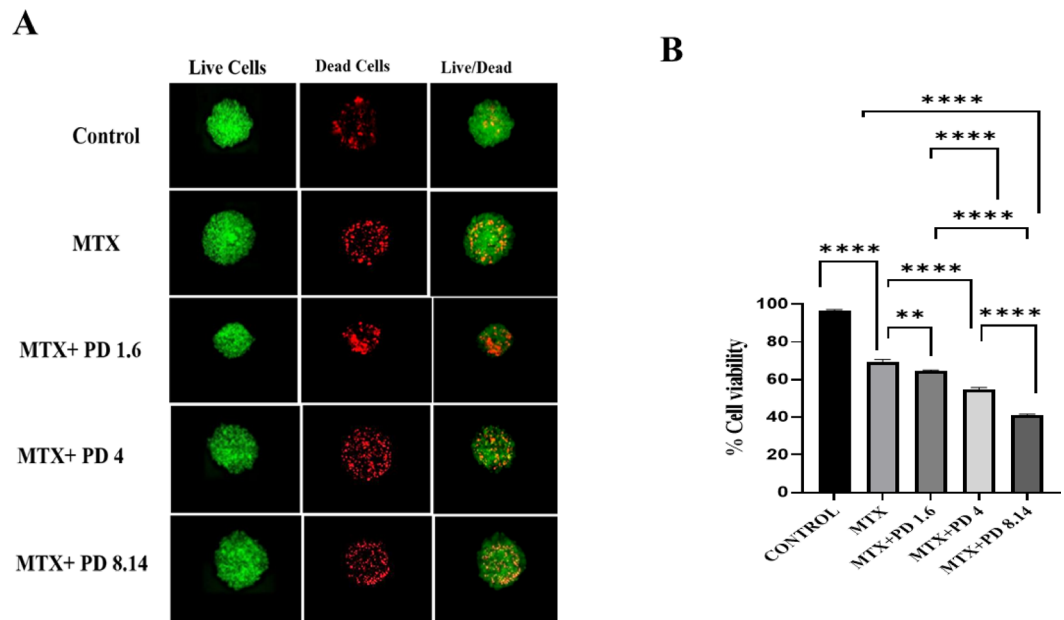
Fig. 6. Live/dead assay for the viability of the HepG2 derived spheroids following treatment with Protodioscin (PD) and Methotrexate (MTX) for 24 h. Green fluorescence indicates Calcein AP stain in the live cells, and red fluorescence indicates the propium iodide stain in the dead cells. **(A)** Quantification from the live/dead assay using ImageJ software. An index of live cells (% of cell viability) was constructed from the ratio of live to total cell numbers. Data from three independent experiments were analyzed and presented as the mean ± SEM. Control (control group), MTX (6 μm), MTX + PD 1.6 (6 μm MTX + 1.6μM PD), MTX + PD 4 (6 μm MTX + 4μM PD) and MTX + PD 8.14 (6 μm MTX + 8.14μM PD).The results are reported as mean ± standard deviation**, and **** demonstrate significant difference between groups at $P < 0.01$ and $p < 0.0001$.

group was significantly higher compared to the 4 μM PD + MTX and 8.14μM PD + MTX groups ($p < 0.05$). The expression of p-Smad2 protein in the 4 μM PD + MTX group did not show any significant difference with the 8.14 μM PD + MTX group (Fig. 8A).

The expression level of p-Smad4 protein in the MTX group was significantly decreased compared to the control group ($p < 0.001$). The expression of p-Smad4 protein in the 1.6, 4 and 8.14 μM PD + MTX groups, was reduced significantly compared to the MTX group ($p < 0.05$, $p < 0.01$, $p < 0.001$). The expression of p-Smad4 protein in the 1.6 μM PD + MTX group was significantly higher compared to the 4 μM PD + MTX and 8.14μM PD + MTX groups ($p < 0.05$, $p < 0.01$). The expression of p-Smad4 protein in the 4 μM PD + MTX group did not show any significant difference with the 8.14 μM PD + MTX group (Fig. 8B).

Discussion

HCC, the most common primary liver cancer, remains a major clinical challenge due to poor prognosis and rising global incidence[45]. Cellular senescence can both limit malignant transformation and promote tumour progression via SASP factors. Residual senescent cells after MTX chemotherapy may contribute to relapse, highlighting senolytic agents as promising adjuvants. Protodioscin (PD), a furostanol-type steroidal saponin from Tribulus terrestris [46,47][46,47], exhibits anticancer effects by inducing apoptosis, inhibiting proliferation, and modulating oncogenic signaling[48,49]. Recently, 3D cell culture models have gained attention for better mimicking the tumour microenvironment compared to 2D systems[50]. Here, we investigated the senolytic potential of PD in a 3D HepG2 spheroid model of MTX-induced senescence, assessing cell death, cell cycle arrest, senescence, and oxidative stress to elucidate its mechanisms.

HepG2 spheroids were generated using the hanging drop method with a 1:1 mixture of complete HepG2 medium and HFF1-conditioned medium, enhancing cell aggregation and viability to produce compact, physiologically relevant spheroids. HFF1 fibroblasts secrete growth factors, cytokines, and extracellular matrix components, supporting HepG2 aggregation, nutrient diffusion, and spheroid compactness[51], thereby providing a microenvironment resembling in vivo liver tumors. Previous studies have shown that PD inhibits cell viability in HCC by inducing apoptosis and cell cycle arrest[38,39]. MTX similarly reduces viability in various cell lines, including HepG2, by inhibiting dihydrofolate reductase and suppressing cell cycle progression[52]. In this study, both MTX and PD decreased HepG2-derived spheroid viability in a dose-dependent manner, with IC$_{50}$ values of 12.25 μM and 16.28 μM at 24 h, respectively. MTX significantly increased NO and ROS production, while PD at 1.6 μM and 4 μM combined with a fixed MTX dose (6 μM) further elevated these reactive species, consistent with previous reports of ROS induction by PD and MTX[36,53]. For instance, MTX has been reported to elevate ROS in HepaRG cells through glutathione (GSH) depletion[54]. At the same time, PD triggers apoptosis in HCC via endoplasmic reticulum stress and oxidative stress mediated by the IP3R signaling pathway[38]. Thus, PD demonstrates a dose-dependent dual behavior—acting as a pro-oxidant at lower concentrations and an
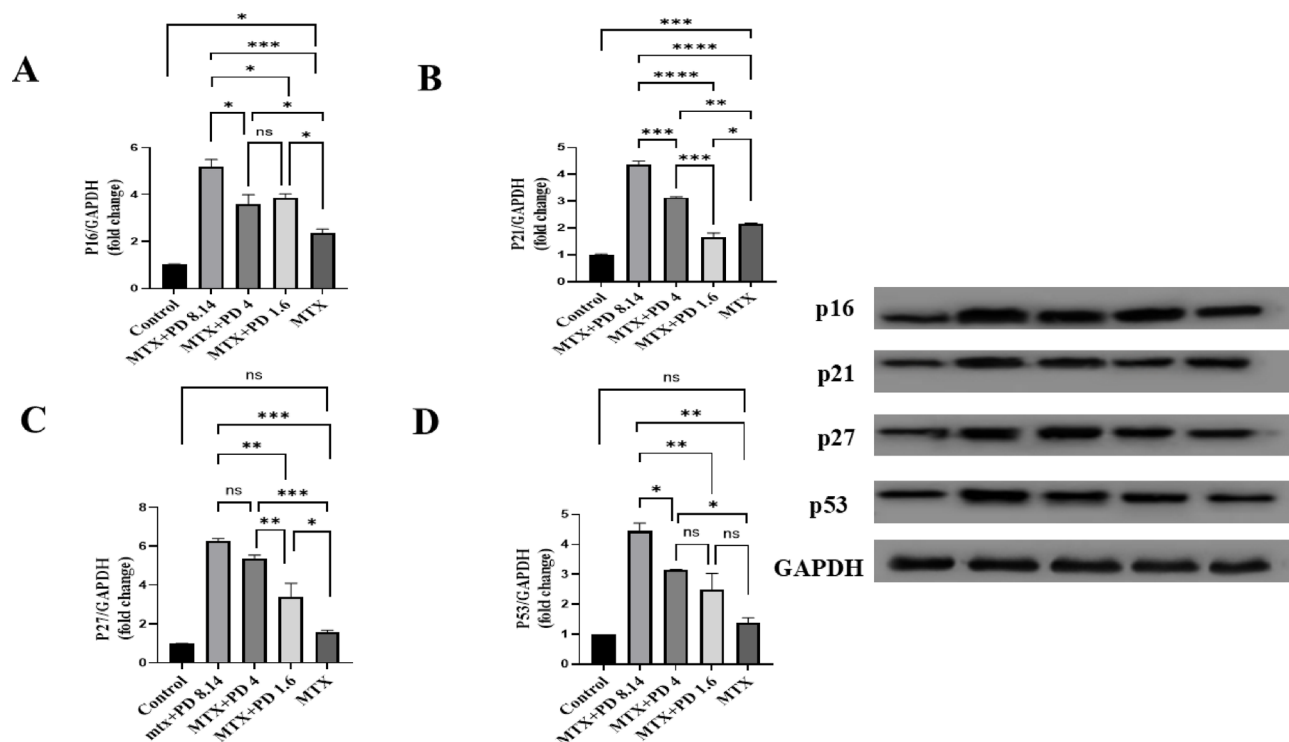
Fig. 7. The expression levels of p16 **(A)**, p21 **(B)**, p27 **(C)**, and p53 **(D)** proteins in HepG2-derived spheroids following 24 h of treatment with Protodioscin (PD) and Methotrexate (MTX) were analyzed using the Western blot method. Control (control group), MTX (6 μm), MTX + PD 1.6 (6 μm MTX + 1.6μM PD), MTX + PD 4 (6 μm MTX + 4μM PD) and MTX + PD 8.14 (6 μm MTX + 8.14μM PD).GAPDH protein was used as a calibrator. The results are reported as mean ± standard deviation for tree replicates. *, **, *** and **** demonstrate significant difference between groups at $P < 0.05$, $P < 0.01$, $p < 0.001$ and $p < 0.0001$.
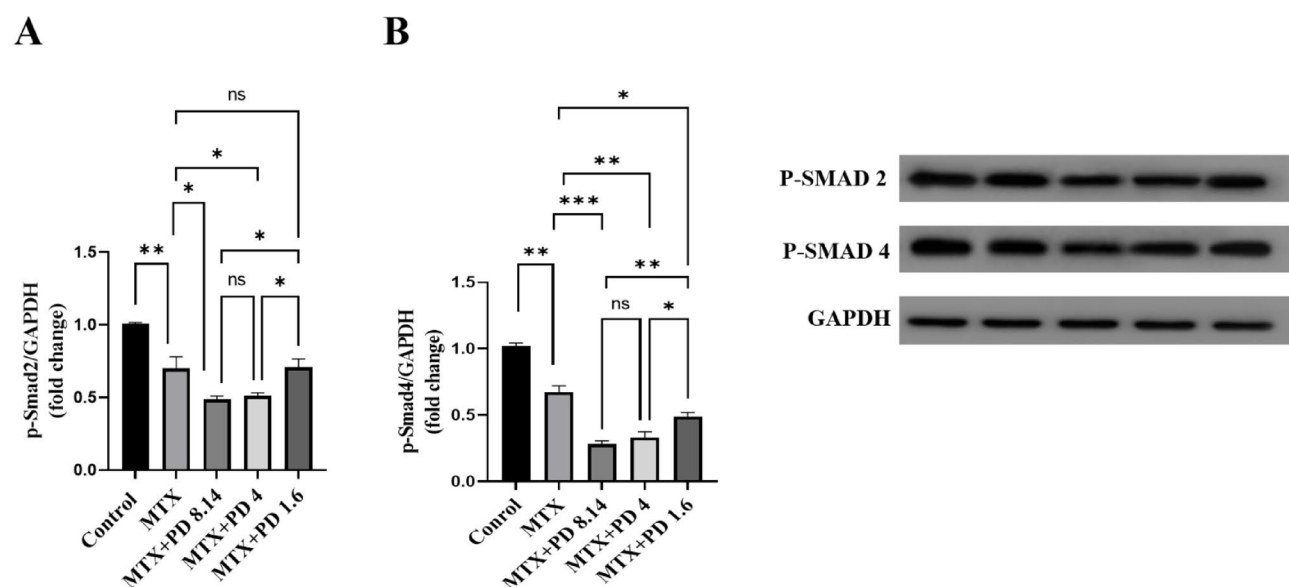
Fig. 8. The expression level of p-Smad2 **(A)** and p-Smad 4 **(B)** proteins in in HepG2-derived spheroids following 24 h of treatment with Protodioscin (PD) and Methotrexate (MTX) were analyzed using the Western blot method. Control (control group), MTX (6 μm), MTX + PD 1.6 (6 μm MTX + 1.6μM PD), MTX + PD 4 (6 μm MTX + 4μM PD) and MTX + PD 8.14 (6 μm MTX + 8.14μM PD).GAPDH protein was used as a calibrator. The results are reported as mean ± standard deviation. *, **, and *** demonstrate significant difference between groups at $P < 0.05$, $P < 0.01$, and $p < 0.001$.

antioxidant at higher concentrations. Such biphasic responses are common among antioxidant-based anticancer agents. Supporting evidence includes findings by Lee et al. (2022), showing that high-dose metformin reduced oxidative stress in renal carcinoma cells by upregulating superoxide dismutase (SOD) and downregulating cyclin D[55]. Moreover, Zargan et al. (2021) found that curcumin reduced NO and enhanced catalase and glutathione levels in 3D MCF-7 cultures[56]. Lee et al. (2021) showed that curcumin treatment reduced B[a]P-induced lipid accumulation and ROS in HepG2 cells[57]. Overall, PD enhances MTX cytotoxicity at low concentrations while mitigating oxidative stress at higher doses, highlighting the importance of dose optimization when using senolytic phytochemicals as chemotherapy adjuvants.

Live/dead and Annexin V/PI assays showed that MTX induced cell death and apoptosis in HepG2-derived spheroids. Co-treatment with a fixed MTX dose and varying PD concentrations revealed a dose-dependent synergistic effect, enhancing cell death and apoptosis. PD induces mitochondrial apoptosis in HCC via ER stress-mediated IP3R-targeted Mfn1/Bak expression and G2/M arrest[38,39]. Additionally, in Hep3B liver cancer cells, MTX combined with vitamin C enhanced oxidative stress and promoted apoptosis by inducing increases in H_2O_2 levels and caspase 9/3 activation[58]. Hamza et al. (2023) showed that the Hibiscus-Cisplatin combination reduced liver toxicity in rats while enhancing oxidative stress and inducing apoptosis in lung cancer cells[59]. This indicates a selective effect that protects normal tissue while promoting cancer cell death. These results support PD as a natural co-therapeutic agent with MTX in 3D HepG2 spheroid models.

Previous studies have shown that methyl PD induces cell cycle arrest and apoptosis in HepG2 cells[39]. Similarly, MTX upregulated p16, p21, p27, and p53, consistent with Spurlock et al. (2012), who reported MTX-induced activation of the JNK pathway and apoptosis via p53, p21, and p27[60]. Co-treatment with PD and MTX further modulated these markers in a dose-dependent manner. PD enhanced p16, p27, and p53 expression, with higher concentrations producing stronger effects. At low PD doses, p21 was reduced compared to MTX alone but increased with higher concentrations. This biphasic pattern suggests that low PD levels mainly promote senescence, while higher doses activate both senescence and apoptosis. Senolytic drugs often act through the p16^INK4a^/Rb pathway[61]. The upregulation of senescence-related proteins observed here supports PD's role in enhancing senescence signaling under MTX-induced stress. Consistent findings were reported by Yi-Long et al. (2019), showing that methyl protodioscin (MPD) induced G2/M arrest and apoptosis via death receptor and mitochondrial pathways[62]. Chen et al. (2023) showed that MPD inhibited the MAPK pathway and induced apoptosis in prostate cancer cells[48]. PD has also shown anti-tumor activity in bladder cancer through JNK and P38 activation, leading to growth inhibition and apoptosis[63]. Overall, PD enhances MTX-induced senolytic and pro-apoptotic effects by modulating cell-cycle regulators and activating multiple death pathways. The dose-dependent induction of p16, p27, and p53—and the variable p21 response—highlight PD's dual influence on senescence and apoptosis, supporting its potential as a senolytic adjuvant in HCC chemotherapy. Although senescence and apoptosis are distinct, they represent interconnected responses to cellular stress. Senescence involves stable cell cycle arrest, elevated β-galactosidase activity, and upregulation of p21 and p16, whereas apoptosis is characterized by caspase activation and programmed cell death[64]. In our study, treatment of MTX-induced senescent HepG2 spheroids with PD initially enhanced senescence-associated signaling, followed by a marked apoptotic response upon prolonged exposure. This suggests that PD first promotes senescence—likely through oxidative and mitochondrial stress—and subsequently triggers apoptosis once cellular damage surpasses repair capacity. Such sequential "senescence-to-apoptosis" transitions have been reported in other cancer models. Pungsrinont et al. (2020) showed that senolytic compounds can shift senescent prostate cancer cells toward apoptosis depending on the inducing signal[65]. Consistent with these findings, our data indicate that PD exerts a dual effect—enhancing senescence under methotrexate stress and later promoting apoptosis—supporting its potential as a senolytic agent capable of eliminating persistently senescent hepatic tumor cells. Our results showed that combined treatment with MTX and PD significantly decreased phosphorylation of p-Smad2 and p-Smad4, accompanied by reduced TGF-β expression in HepG2 spheroids. Since Smad2/4 phosphorylation is required for Smad complex activation and nuclear translocation, this reduction indicates that PD attenuates TGF-β signaling at both receptor and transcriptional levels. Given the dual role of TGF-β in cancer, its downregulation may contribute to reduced tumor growth and invasion[13]. By suppressing TGF-β and p-Smad2/4, PD may shift signaling toward growth arrest and apoptosis rather than invasion. TGF-β upregulates p15, p21, and p27 via Smad-responsive promoters. However, in our study, inhibition of TGF-β/Smad signaling coincided with increased p16, p21, and p27 expression. This pattern suggests activation of TGF-β–independent checkpoints commonly engaged under senescence or stress conditions[66,67]. Supporting this, previous studies have shown that several Smad-independent mechanisms regulate CDK inhibitors. The p53–p21 axis can be activated by ROS-driven ATM/ATR signaling, leading to p21 induction independent of Smad input. Likewise, the FOXO3a transcription factor directly activates p27 even when TGF-β is suppressed[68]. Activation of the p38 MAPK pathway under oxidative or mitochondrial stress also promotes senescence and elevates p16 and p21 independently of TGF-β signalling[69]. Zhong et al. indicated that downregulation of SKP2 stabilizes p27 by reducing its ubiquitin-mediated degradation, maintaining growth arrest irrespective of Smad activity[70]. Cell-cycle arrest in senescence is mainly mediated through p53/p21^WAF1/CIP1^ and p16^INK4A^/pRB pathways, which sustain the senescent state by regulating transcriptional networks. While p21 acts downstream of p53, p16 functions within the RB/E2F checkpoint rather than as a direct Smad target. Pathways such as ATM/ATR/p53 and p38 MAPK may reinforce RB/E2F repression and enhance p16 expression, thereby promoting senescence. Collectively, these findings suggest that in MTX-treated HepG2 spheroids, the PD-induced elevation of p16, p21, and p27—despite reduced TGF-β and Smad phosphorylation—likely occurs through Smad-independent stress pathways. Further studies are warranted to clarify the alternative mechanisms underlying PD's senolytic activity in HepG2 cells. TGF-β signaling exhibits a paradoxical role in cancer: it acts as a tumor suppressor in early tumorigenesis but promotes progression in advanced cancers via EMT induction. This duality arises from alterations in Smad signaling, cross-talk with oncogenic pathways, and changes in the tumor

microenvironment[71]. In our study, co-treatment with PD and MTX significantly reduced TGF-β expression and p-Smad2/4 phosphorylation, accompanied by decreased cell viability and upregulation of senescence- and apoptosis-related markers. Although EMT markers were not directly assessed, these findings suggest that PD primarily interferes with the pro-survival and pro-metastatic aspects of TGF-β signaling, favoring tumor-suppressive and senolytic outcomes. Future studies should evaluate EMT-related targets to clarify PD's effects on the balance between EMT and senescence.

Our results also indicate a dose-dependent dual effect of PD on oxidative stress and TGF-β/p-Smad signaling. At low concentrations, PD increased ROS, while at higher doses, ROS, TGF-β expression, and Smad2/4 phosphorylation were reduced. This biphasic response reflects the dual role of ROS in TGF-β regulation: moderate ROS activate latent TGF-β complexes and promote Smad phosphorylation via redox-sensitive kinases such as p38 MAPK and JNK, whereas excessive ROS inhibits TβRII and Smad3 phosphorylation[72]. In addition, NO directly S-nitrosylates cysteine residues in the C-terminal region of TGF-β1, decreasing its signaling activity[73]. In cancer cells, TGF-β and ROS form a feed-forward loop; high-dose PD disrupts this loop through antioxidant and radical-scavenging activity, concurrently inhibiting ROS and TGF-β/p-Smad signaling. Collectively, these findings indicate that PD modulates TGF-β/p-Smad signaling in a redox-dependent, biphasic manner—acting as a pro-oxidant at low doses and an antioxidant at high doses. Our results showed that MTX induced cellular senescence in HepG2 spheroids, as evidenced by SAβ-Gal staining, and co-treatment with PD further enhanced this effect. While PD is mainly known for pro-apoptotic and anti-proliferative roles, it can also promote senescence via ER stress, mitochondrial dysfunction, and ROS-dependent pathways[36]. Consistently, in 3D culture, PD activated growth arrest and senescence-associated pathways, similar to other natural bioactive compounds like food-derived peptides[74]. Further investigation of signaling pathways and specific senescence markers is warranted to clarify the underlying molecular mechanisms.

Summary of strengths, limitations, and future directions

This study highlights the senolytic and anti-metastatic potential of PD in HCC using 3D spheroid models, providing a more physiologically relevant platform compared to 2D cultures. The comprehensive evaluation of PD's dose-dependent effects on apoptosis, oxidative stress, and senescence represents a key strength. However, the findings are limited to in vitro analyses, and the molecular mechanisms underlying PD's dual pro-senescent and senolytic actions remain to be fully elucidated. Future investigations should validate epithelial–mesenchymal transition (E-cadherin, vimentin) and SASP cytokines (IL-6, IL-8, TNF-α) to confirm PD's role in modulating TGF-β signaling. In vivo studies and dose-optimization analyses are also warranted to determine whether the observed dose-dependent interactions between PD and MTX can be recapitulated under physiological conditions.

Conclusion

Our findings highlight the therapeutic potential of PD as a senolytic agent in HCC. In 3D HepG2 spheroids, PD induced dose-dependent cell cycle arrest, cell death, apoptosis, oxidative stress, and senescence. Co-treatment with MTX and PD also induced senescence, indicating a dual role in tumor cell fate (Fig. 9). At higher doses, PD antagonized MTX-induced oxidative stress, showing a dose-dependent shift from synergistic to antagonistic effects. Importantly, combination therapy inhibited the TGF-β/p-Smad pathway, suppressed extracellular matrix production, and reduced tumor invasion. We propose that co-treatment of MTX and PD may serve as a more effective strategy for treating hepatocellular carcinoma through induction of cellular senescence and concurrent senolytic activity.
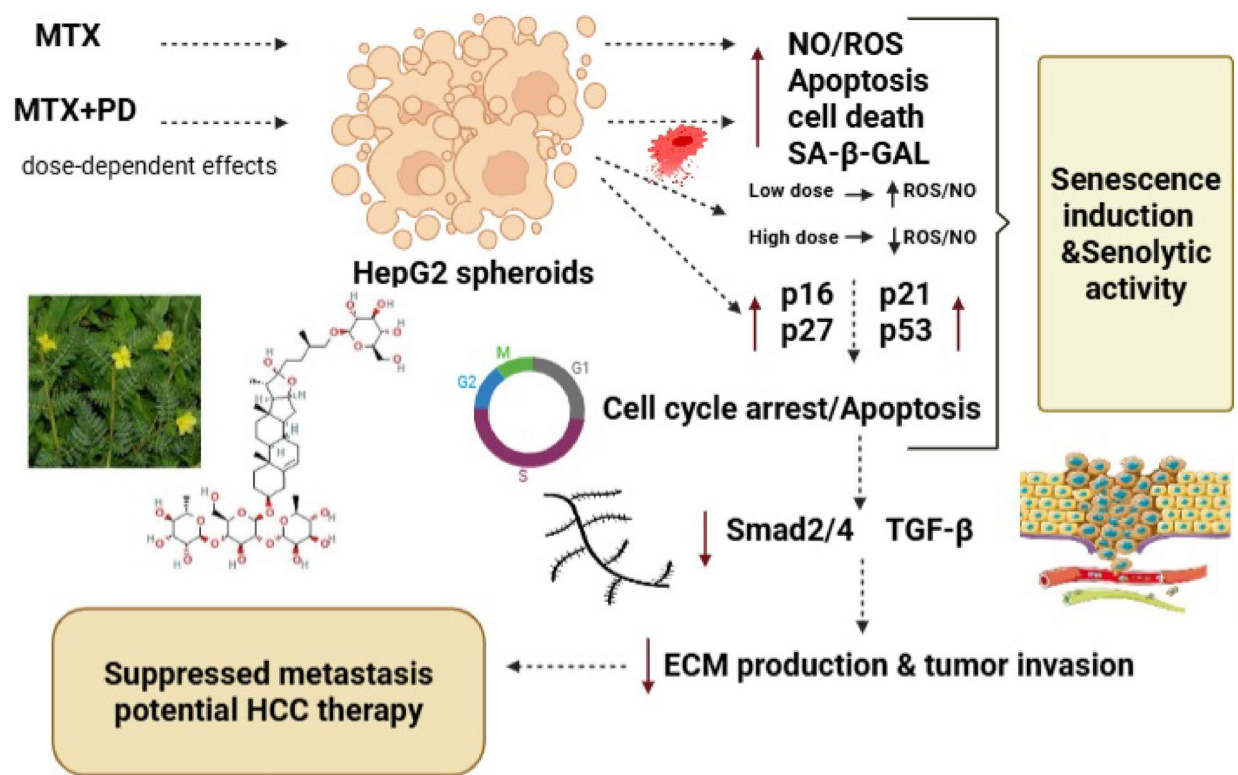
Fig. 9. Schematic representation illustrating the senolytic effects of PD on MTX-treated HepG2 spheroids, highlighting changes in ROS/NO levels, apoptosis, SA-β-Gal activity, cell cycle regulators, and TGF-β/Smad2/4 signaling pathways.

Refrences

1. Rumgay, H. et al. Global burden of primary liver cancer in 2020 and predictions to 2040. *J. Hepatol.* **77**, 1598–1606 (2022).
2. Alamri, Z. Z. The role of liver in metabolism: an updated review with physiological emphasis. *Int. J. Basic. Clin. Pharmacol.* **7**, 2271–2276 (2018).
3. Hamed, K. M. et al. Overview of methotrexate toxicity: a comprehensive literature review. *Cureus* **14** (2022).
4. Dabrowska, M., Uram, L., Dabrowski, M. & Sikora, E. Antigen presentation capability and AP-1 activation accompany methotrexate-induced colon cancer cell senescence in the context of aberrant β-catenin signaling. *Mech. Ageing Dev.* **197**, 111517 (2021).
5. Gazzillo, A. et al. Cellular senescence in liver cancer: how dying cells become zombie enemies. *Biomedicines* **12**, 26 (2023).
6. Dabrowska, M., Mosieniak, G., Skierski, J., Sikora, E. & Rode, W. Methotrexate-induced senescence in human adenocarcinoma cells is accompanied by induction of p21waf1/cip1 expression and lack of polyploidy. *Cancer Lett.* **284**, 95–101 (2009).
7. Dong, Z. et al. Cellular senescence and SASP in tumor progression and therapeutic opportunities. *Mol. Cancer.* **23**, 181 (2024).
8. Pretto, L., Nabinger, E., Filippi-Chiela, E. C. & Fraga, L. R. Cellular senescence in reproduction: a two-edged sword. *Biol. Reprod.* **110**, 660–671 (2024).
9. Kumari, R. & Jat, P. Mechanisms of cellular senescence: cell cycle arrest and senescence associated secretory phenotype. *Front. cell. Dev. Biology.* **9**, 645593 (2021).
10. González-Gualda, E., Baker, A. G., Fruk, L. & Muñoz-Espín D. A guide to assessing cellular senescence in vitro and in vivo. *FEBS J.* **288**, 56–80 (2021).
11. Karabicici, M., Alptekin, S., Fırtına Karagonlar, Z. & Erdal, E. Doxorubicin-induced senescence promotes stemness and tumorigenicity in EpCAM–/CD133– nonstem cell population in hepatocellular carcinoma cell line, HuH-7. *Mol. Oncol.* **15**, 2185–2202 (2021).
12. Aashaq, S. et al. TGF-β signaling: A recap of SMAD-independent and SMAD-dependent pathways. *J. Cell. Physiol.* **237**, 59–85 (2022).
13. Li, X., Wu, Y. & Tian, T. TGF-β signaling in metastatic colorectal cancer (mCRC): from underlying mechanism to potential applications in clinical development. *Int. J. Mol. Sci.* **23**, 14436 (2022).
14. Xu, J., Lamouille, S. & Derynck, R. TGF-β-induced epithelial to mesenchymal transition. *Cell Res.* **19**, 156–172 (2009).
15. Coppé, J. P., Desprez, P. Y., Krtolica, A. & Campisi, J. The senescence-associated secretory phenotype: the dark side of tumor suppression. *Annu. Rev. Pathol.* **5**, 99–118 (2010).
16. Takasugi, M., Yoshida, Y. & Ohtani, N. Cellular senescence and the tumour microenvironment. *Mol. Oncol.* **16**, 3333–3351 (2022).

17. Li, D. et al. Interactions between oxidative stress and senescence in cancer: mechanisms, therapeutic implications, and future perspectives. *Redox Biol.* **73**, 103208 (2024).

18. Pakuła, M. et al. Deciphering the molecular mechanism of spontaneous senescence in primary epithelial ovarian cancer cells. *Cancers* **12**, 296 (2020).

19. George, N., Joshi, M. B. & Satyamoorthy, K. DNA damage-induced senescence is associated with metabolomic reprogramming in breast cancer cells. *Biochimie* **216**, 71–82 (2024).

20. Rysanek, D. et al. Synergism of BCL-2 family inhibitors facilitates selective elimination of senescent cells. *Aging (Albany NY).* **14**, 6381 (2022).

21. Fan, Z. et al. Inhibitor PF-04691502 works as a senolytic to regulate cellular senescence. *Exp. Gerontol.* **186**, 112359 (2024).

22. Lee, S. & Lee, J. S. Cellular senescence: a promising strategy for cancer therapy. *BMB Rep.* **52**, 35 (2019).

23. Reimann, M. et al. Tumor stroma-derived TGF-β limits myc-driven lymphomagenesis via Suv39h1-dependent senescence. *Cancer cell.* **17**, 262–272 (2010).

24. Ueda, S. et al. TGF-β1 is involved in senescence-related pathways in glomerular endothelial cells via p16 translocation and p21 induction. *Sci. Rep.* **11**, 21643 (2021).

25. Chin, A. F. et al. Senolytic treatment reduces oxidative protein stress in an aging male murine model of post-traumatic osteoarthritis. *Aging Cell.* **22**, e13979 (2023).

26. Zhu, Y. et al. The achilles' heel of senescent cells: from transcriptome to senolytic drugs. *Aging cell.* **14**, 644–658 (2015).

27. Awad, B., Hamza, A. A., Al-Maktoum, A., Al-Salam, S. & Amin, A. Combining Crocin and Sorafenib improves their tumor-inhibiting effects in a rat model of diethylnitrosamine-induced cirrhotic-hepatocellular carcinoma. *Cancers* **15**, 4063 (2023).

28. Ismail, R., Habib, H. A., Anter, A. F., Amin, A. & Heeba, G. H. Modified citrus pectin ameliorates methotrexate-induced hepatic and pulmonary toxicity: role of Nrf2, galectin-3/TLR-4/NF-κB/TNF-α and TGF-β signaling pathways. *Front. Pharmacol.* **16**, 1528978 (2025).

29. Montero, J. C., Seoane, S., Ocaña, A. & Pandiella, A. Inhibition of SRC family kinases and receptor tyrosine kinases by dasatinib: possible combinations in solid tumors. *Clin. Cancer Res.* **17**, 5546–5552 (2011).

30. Wang, L. et al. Senolytic drugs dasatinib and Quercetin combined with carboplatin or Olaparib reduced the peritoneal and adipose tissue metastasis of ovarian cancer. *Biomed. Pharmacother.* **174**, 116474 (2024).

31. Chang, J. et al. Clearance of senescent cells by ABT263 rejuvenates aged hematopoietic stem cells in mice. *Nat. Med.* **22**, 78–83 (2016).

32. Chen, X. et al. Protective effects of Methyl Protodioscin against lipid disorders and liver injury in hyperlipidemic gerbils. *Heliyon* **9** (2023).

33. Shu, K. & Zhang, Y. Protodioscin protects PC12 cells against oxygen and glucose deprivation-induced injury through miR-124/AKT/Nrf2 pathway. *Cell. Stress Chaperones.* **24**, 1091–1099 (2019).

34. Zhang, X. et al. Potential neuroprotection of Protodioscin against cerebral ischemia-reperfusion injury in rats through intervening inflammation and apoptosis. *Steroids* **113**, 52–63 (2016).

35. Chen, Y. R. et al. Protodioscin inhibits bladder cancer cell migration and growth, and promotes apoptosis through activating JNK and p38 signaling pathways. *Biomed. Pharmacother.* **156**, 113929 (2022).

36. Lin, C. L. et al. Protodioscin induces apoptosis through ROS-mediated Endoplasmic reticulum stress via the JNK/p38 activation pathways in human cervical cancer cells. *Cell. Physiol. Biochem.* **46**, 322–334 (2018).

37. Hu, K. & Yao, X. The cytotoxicity of Methyl Protodioscin against human cancer cell lines in vitro. *Cancer Invest.* **21**, 389–393 (2003).

38. Yu, C. L. et al. Protodioscin induces mitochondrial apoptosis of human hepatocellular carcinoma cells through eliciting ER stress-mediated IP3R targeting Mfn1/Bak expression. *Journal Hepatocellular Carcinoma*, 327–341 (2022).

39. Wang, G. et al. Methyl Protodioscin induces G2/M cell cycle arrest and apoptosis in HepG2 liver cancer cells. *Cancer Lett.* **241**, 102–109 (2006).

40. Phung, Y. T., Barbone, D., Broaddus, V. C. & Ho, M. Rapid generation of in vitro multicellular spheroids for the study of monoclonal antibody therapy. *J. Cancer.* **2**, 507 (2011).

41. Al Hrout, A., Cervantes-Gracia, K., Chahwan, R. & Amin, A. Modelling liver cancer microenvironment using a novel 3D culture system. *Sci. Rep.* **12**, 8003 (2022).

42. Bartosh, T. et al. (ed, J.) Aggregation of human mesenchymal stromal cells (MSCs) into 3D spheroids enhances their antiinflammatory properties. *Proc. Natl. Acad. Sci.* **107** 13724–13729 (2010).

43. Zhang, X., Hu, M. G., Pan, K., Li, C. H. & Liu,. 3D spheroid culture enhances the expression of antifibrotic factors in human adipose-derived MSCs and improves their therapeutic effects on hepatic fibrosis. *Stem Cells Int.* **2016**, 4626073 (2016).

44. Phour, J. & Vassella, E. Methods in cancer research: assessing therapy response of spheroid cultures by life cell imaging using a cost-effective live-dead staining protocol. *Biology Methods Protocols.* **9**, bpae060 (2024).

45. Anwanwan, D., Singh, S. K., Singh, S., Saikam, V. & Singh, R. Challenges in liver cancer and possible treatment approaches. *Biochim. Biophys. Acta Rev. Cancer.* **1873**, 188314 (2020).

46. Shishovska, M., Arsova-Sarafinovska, Z. & Memeti, S. A simple method for determination of Protodioscin in tribulus terrestris L. and pharmaceuticals by high performance liquid chromatography using Diode-Array detection. *J. Chem. Eng. Res. Updates.* **2**, 12–21 (2015).

47. Zhang, R. S. et al. Furostanol saponins from asparagus cochinchinensis and their cytotoxicity. *Nat. Prod. Bioprospecting.* **11**, 651–658 (2021).

48. Chen, J. et al. Anticancer activity of Methyl Protodioscin against prostate cancer by modulation of cholesterol-associated MAPK signaling pathway via FOXO1 induction. *Biol. Pharm. Bull.* **46**, 574–585 (2023).

49. Bouchmaa, N. et al. In vitro evaluation of Dioscin and Protodioscin against ER-positive and triple-negative breast cancer. *PloS One.* **18**, e0272781 (2023).

50. Zhu, Y. et al. 3D tumor spheroid and organoid to model tumor microenvironment for cancer immunotherapy. *Organoids* **1**, 149–167 (2022).

51. Barbosa, M. A., Xavier, C. P., Pereira, R. F., Petrikaitė, V. & Vasconcelos, M. H. 3D cell culture models as recapitulators of the tumor microenvironment for the screening of anti-cancer drugs. *Cancers* **14**, 190 (2021).

52. Wang, Y. et al. Metformin sensitises hepatocarcinoma cells to methotrexate by targeting dihydrofolate reductase. *Cell Death Dis.* **12**, 902 (2021).

53. AlBasher, G. et al. Methotrexate-induced apoptosis in human ovarian adenocarcinoma SKOV-3 cells via ROS-mediated bax/bcl-2-cyt-c release cascading. *OncoTargets Therapy*, 21–30 (2018).

54. Schmidt, S., Messner, C. J., Gaiser, C. & Hämmerli, C. Suter-Dick, L. Methotrexate-induced liver injury is associated with oxidative stress, impaired mitochondrial respiration, and Endoplasmic reticulum stress in vitro. *Int. J. Mol. Sci.* **23**, 15116 (2022).

55. Liu, Y., Li, J., Song, M., Qi, G. & Meng, L. High-concentration metformin reduces oxidative stress injury and inhibits the growth and migration of clear cell renal cell carcinoma. *Comput. Math. Methods Med.* **2022**, 1466991 (2022).

56. Zargan, S. et al. Evaluation of the anti-cancer effect of Curcumin on MCF-7 cells in 3D culture conditions to increase the efficacy of breast cancer treatment. *J. Appl. Biotechnol. Rep.* **9**, 547–556 (2022).

57. Lee, S. C. et al. Curcumin suppresses the lipid accumulation and oxidative stress induced by benzo [a] pyrene toxicity in HepG2 cells. *Antioxidants* **10**, 1314 (2021).

58. Yiang, G. T. et al. Vitamin C enhances anticancer activity in methotrexate-treated Hep3B hepatocellular carcinoma cells. *Oncol. Rep.* **32**, 1057–1063 (2014).
59. Hamza, A. A. et al. Hibiscus-cisplatin combination treatment decreases liver toxicity in rats while increasing toxicity in lung cancer cells via oxidative stress-apoptosis pathway. *Biomed. Pharmacother.* **165**, 115148 (2023).
60. Spurlock, I. I. I., Tossberg, C. F., Fuchs, J. T., Olsen, H. A., Aune, T. M. & N. J. & Methotrexate increases expression of cell cycle checkpoint genes via JNK activation. *Arthr. Rhuem.* **64**, 1780–1789 (2012).
61. Carpenter, V. J., Saleh, T. & Gewirtz, D. A. Senolytics for cancer therapy: is all that glitters really gold? *Cancers* **13**, 723 (2021).
62. Ma, Y. L. et al. Methyl Protodioscin from polygonatum sibiricum inhibits cervical cancer through cell cycle arrest and apoptosis induction. *Food Chem. Toxicol.* **132**, 110655 (2019).
63. Kim, S. H. et al. Protodioscin protects Porcine oocytes against H2O2-induced oxidative stress during in vitro maturation. *Anim. Bioscience.* **36**, 710 (2022).
64. Jan, N., Sofi, S., Mir, A. A., Masoodi, G. & Mir, M. A. Balancing senescence and apoptosis: therapeutic insights into aging and cancer. *Molecular Cell. Biochemistry*, 1–30 (2025).
65. Pungsrinont, T. et al. Senolytic compounds control a distinct fate of androgen receptor agonist-and antagonist-induced cellular senescent LNCaP prostate cancer cells. *Cell. Bioscience.* **10**, 59 (2020).
66. Gungor, M. Z., Uysal, M. & Senturk, S. The bright and the dark side of TGF-β signaling in hepatocellular carcinoma: mechanisms, dysregulation, and therapeutic implications. *Cancers* **14**, 940 (2022).
67. Tewari, D., Priya, A., Bishayee, A. & Bishayee, A. Targeting transforming growth factor-ß signalling for cancer prevention and intervention: recent advances in developing small molecules of natural origin. *Clin. Translational Med.* **12**, e795 (2022).
68. Lees, S. J., Childs, T. E. & Booth, F. W. Age-dependent FOXO regulation of p27Kip1 expression via a conserved binding motif in rat muscle precursor cells. *Am. J. Physiology-Cell Physiol.* **295**, C1238–C1246 (2008).
69. González-Osuna, L. et al. p38 mitogen-activated protein kinase drives senescence in CD4 + T lymphocytes and increases their pathological potential. *Immun. Ageing.* **22**, 1–14 (2025).
70. Zhong, L. et al. Essential role of Skp2-mediated p27 degradation in growth and adaptive expansion of pancreatic β cells. *J. Clin. Investig.* **117**, 2869–2876 (2007).
71. Seoane, J & Gomis, R. R. TGF-β family signaling in tumor suppression and cancer progression. *Cold Spring Harb. Perspect. Biol.* **9**, a022277 (2017).
72. He, T., Quan, T., Shao, Y., Voorhees, J. J. & Fisher, G. J. Oxidative exposure impairs TGF-β pathway via reduction of type II receptor and SMAD3 in human skin fibroblasts. *Age* **36**, 9623 (2014).
73. Letson, J. et al. Reduced S-nitrosylation of TGFβ1 elevates its binding affinity toward the receptor and promotes fibrogenic signaling in the breast. *Journal Biol. Chemistry* **300** (2024).
74. Hamdi, M. et al. Bioactive peptides with potential anticancer properties from various food protein sources: status of recent research, production technologies, and developments. *Critical Reviews Biotechnology*, 1–22 (2025).

Author contributions
A. JS.: Conceptualization, Methodology. A.G: Data curation, Visualization. MR.T: Writing – Review & Editing, and data interpretation. A. F: Formal analysis. F. M: Investigation, Validation. T. Z N: Writing – Original Draft,: Software. C. J: conceptualization, Supervision, Project administration, Writing – Review & Editing. All authors reviewed the manuscript.

Declarations

Competing interests
The authors declare no competing interests.

Ethics approval and consent to participate

Additional information
Supplementary Information The online version contains supplementary material available at https://doi.org/1 0.1038/s41598-025-27926-6.

Correspondence and requests for materials should be addressed to C.J.

Reprints and permissions information is available at www.nature.com/reprints.

Publisher's note Springer Nature remains neutral with regard to jurisdictional claims in published maps and institutional affiliations.